EAST EUROPEAN JOURNAL OF PHYSICS. 3. 415-431 (2026)
DOI:10.26565/2312-4334-2026-3-38 ISSN 2312-4334

INFLUENCE OF HALL CURRENT, THERMAL DISPERSION, AND HEAT GENERATION ON KEROSENE-BASED TiO_2 NANOFLUID FLOW THROUGH A ROTATING POROUS CHANNEL

Venkateswarlu Malapati[1#], Mohammed Almakki[2##], V.B. Rajakumar Komaravolu[3]*
[1]Department of Mathematics, Siddhartha Academy of Higher Education, Vijayawada, Andhra Pradesh, India - 520007
[2]School of Engineering, Architecture and Interior Design, Amity University, Dubai International Academic City, P.O. Box 345019
[3]Department of Mathematics, Kallam Haranadhareddy Institute of Technology, Guntur, Andhra Pradesh, India-522019
[#]Email: mvsr2010@gmail.com, [##]Email: m.almakki1977@gmail.com
*Corresponding Author email: kvbrajakumar@gmail.com
Received May 11, 2026; revised June 19, 2026; accepted June 24, 2026

In contrast to heat generation and thermal dispersal, the Hall current and rotation factors of a kerosene-based titanium dioxide nanoliquid discharge across two parallel walls embedded in a porous channel are inspected. Suction and hydromagnetic factors are contemplated. Using appropriate initial and boundary conditions, the perturbation approach can yield a precise analytical solution to the governing equations for the nanofluid velocity, temperature, and concentration. Expressions for the shear stress, mass transfer rate, and heat transfer rate at the plates can be obtained. On the one hand, a graphical representation of the primary and secondary velocities, the nanoliquid temperature, and the species concentration is shown. However, for distinct values of the related flow factors, the numerical estimates of shear stress, mass transfer rate, and heat transfer rate for the walls are presented in tabular form. Because of the solute buoyancy force's contribution, the resulting primary and secondary velocity profiles continuously rise to a high level. The concentration increases in conjunction with increases in heat generation and thermal diffusion characteristics throughout the nanofluid. When the thermal buoyancy force is high enough, the primary and secondary velocity profiles diminish. Hall current and the Darcy parameter raise the primary and secondary skin friction coefficients at the upper wall while decreasing them at the lower wall. However, the primary and secondary skin friction coefficients are affected in opposite ways by thermal buoyancy force and magnetic parameter. Results are compared with existing literature.
Keywords: *Nanofluid; Couette flow; Hall current; Heat generation; Suction*

1. INTRODUCTION

In both theoretical and practical fluid mechanics, the study of nanofluid flow between two parallel plates is crucial. A basic model for comprehending complicated fluid dynamics in constrained geometries is this flow arrangement, which is frequently referred to as Couette flow. Its importance arises from its many uses, ranging from temperature control in heat exchangers, where it improves heat transfer efficiency, to lubrication technology, where it aids in the design of effective systems to lower friction and wear in mechanical components. Particularly in the field of biomedical engineering, understanding disk flow is crucial for maximizing the efficiency of systems like centrifugal blood pumps, which depend on regulated fluid dynamics. The generalized Couette flow of nanoliquid between two concentric channels with particle injection has been examined by Soumya et al. [1]. The impact of radiating heat and nanoparticle concentration on the natural convection Couette flow via a vertical channel was discussed by Swain et al. [2]. Heat transfer and the Couette flow of viscoelastic dusty fluid via a porous oscillating plate in a rotating frame have been studied by Ali et al. [3]. The thermodynamic study of Hall current and thermal diffusion on hydromagnetic Couette flow in a rotating system with a convective boundary condition was conducted by Venkateswarlu et al. [4]. Heat transfer increase of nanofluids in Taylor-Couette flow with an elliptical slit surface has been examined using machine learning and numerical simulation by Sun et al. [5]. The mathematical modeling of nonlinear mixed convection unsteady flow in a parallel plate inclined channel near time periodic boundary conditions was provided by Venkateswarlu et al. [6]. Gupta [7] used a differential transform approach to examine the effects of volume fraction, squeezing, and magnetic field on MHD nanofluid flow. The temperature and mass dispersion of mixed convective MHD Casson nanofluid flow in a porous medium has been examined by Arpitha et al. [8].

Two types of thermal diffusion phenomena that take place in fluid systems are the Dufour and Soret characteristics. The Soret effect is a technique that separates a liquid combination into its component parts by creating a solutal gradient in the mixture because of a temperature gradient. Another name for this phenomenon is thermal diffusion. The study of combustion processes is where the Soret effect is most evident because it is crucial in determining the chemical composition of the combustion products. A comparable phenomenon is the Dufour effect, which causes a temperature rise in a liquid mixture caused by a solutal gradient. Solute diffusion is the term used to describe this process. Heat and mass transmission are two kinds of transport processes that can be studied using the Dufour effect. Chemical engineering, physics, and biology all make extensive use of these effects. They can be applied, for instance, to protein dynamics analysis, gas purification, and isotope separation. Given their wide range of utilizes in chemical synthesis, pharmacology, and biotechnology, the Soret-Dufour effects must also be considered while designing microfluidic devices. The magnetized dissipative Soret effect on nonlinear radiative Maxwell nanofluid flow

Cite as: V. Malapati, M. Almakki, V.B.R. Komaravolu, East Eur. J. Phys. 3, 415 (2026), https://doi.org/10.26565/2312-4334-2026-3-38

with porosity, chemical reaction, and Joule heating was described by Bayones et al. [9]. The Newtonian fluid flow with heat and mass transfer across an inclined sheet and magnetic field with Soret effects was described by Mudoi et al. [10]. The velocity slip and magnetic Soret effect on dissipative Maxwell liquid motion around a stretching wall with a heat source and sink were examined by Basha et al. [11]. The Soret and Dufour effects on heat-destructive Casson liquid movement past an infinite perpendicular plate were studied by Venkateswarlu et al. [12]. The implications of heat sources and chemical responses on oscillatory suction in MHD flow by means of permeable medium with the Soret phenomenon were discussed by Pandey [13]. Using an artificial neural network, Jangid and Kolla [14] described the Soret impact and magnetic field on a mixed convection Williamson fluid model across a vertical channel. The consequences of Soret and Dufour characteristics on micropolar fluid passing a stretched sheet in a porous media were reported by Ahamed sheriff et al. [15]. Utilizing a chemically reacting porous stretching plate, Sarma et al. [16] explored the MHD flow and the impacts of Soret, Dufour, and thermophoresis. The significant advancements in our knowledge of fluid flow with Soret and Dufour effects are shown in the publications Venkateswarlu and Venkata Lakshmi [17, 18], Makinde et al. [19], Jayanthi and Niranjan [20], and Venkateswarlu and Phani Kumar [21].

Magnetism, one of the most crucial concepts in engineering and manufacturing, has a wide range of uses. Heat transmission, clutches, compressors, as well as other industrial devices are all impacted by magnetic fields and fluid nanoparticles. Magnetic fields can modify and make available the cooling rate of various technical devices. The dispersion and strength of a metamaterial affect the flow characteristics. The unstable MHD slip flow with radiative heat and mass transfer across an inclined plate embedded in a porous medium was described by Venkateswarlu and Makinde [22]. Heat generation and magnetic consequences of unsteady ternary nanofluid flow across a dynamic wedge in porous media were examined by Ouyang et al. [23]. The thermo-solutal nonlinear convection in a nanofluid movement via a porous plate including heat generation and absorption was studied by Dey et al. [24]. In a double lid-driven inclined wavy porous cavity filled with non-Newtonian nanofluid and equipped with a cross-shaped heater, Hussein et al. [25] described the effects of radiation and heat generation on MHD mixed convection. In an inclined plate near MHD and heat generation, Venkateswarlu et al. [26] investigated the impulsive and accelerated motions of Casson fluid. Radiative heat transfer and Ohmic heating on unstable EMHD mixed convective flow for dual stratification nanofluid were described by Daniel et al. [27]. In an inclined stenotic artery with heat generation, Kefene and Rikitu [28] described the implications of magnetic and thermal radiation on hematocrit-dependent blood nanofluid movement. In an inclined channel with suction and heat generation, Venkateswarlu et al. [29] explored the non-linear unstable MHD flow. The stagnation point motion of a magnetized convective nanofluid across a porous stretchable surface according to ohmic heating and heat generation was described by Ram et al. [30]. The significance of cross-section diffusion on the transient behavior of radiation Casson fluid towards a heated slanted plate was examined by Venkateswarlu et al. [31].

The corpus of published work indicates that no author has yet examined the factors of thermal dispersal, Hall current, and heat generation of an unsteady titanium dioxide nanofluid flow across a parallel porous tunnel. Exploring the hydromagnetic flow of a titanium dioxide nanofluid in a horizontal tunnel via a porous media is the goal of this work. The extraction of oil from hydrocarbon deposits, the fabrication of semiconductor devices from molten metal, solar energy structures, electronic device cooling, and environmental remediation are just a few of the many real-world applications for this study.

2. MATHEMATICAL FRAMEWORK

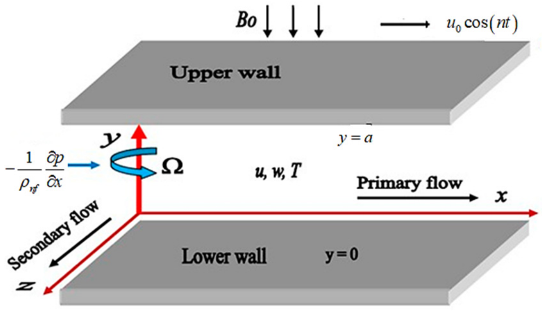

Figure 1. Flow geometry is depicted

The unstable Couette flow of a titanium dioxide nanoliquid based on kerosene across two parallel walls, $y = 0$ and $y = a$, is examined when a uniform transversal magnetic field B_0 is enforced parallel to the $y-$axis while incorporating the Hall current. The nanofluid and tunnel rotate continuously across the $y-$axis at a constant angular velocity Ω. The impact of radial strength is minimal because of nanofluid axial Couette flow motion, but the bending impact of Coriolis strength acting orthogonal to the direction of nanofluid movement and to the axis of rotating allusion structure is taken into concern. The effects of heat emission and thermal dispersion are considered. The invariable pressure gradient applied along the $x-$direction and the motion of the upper wall with systematic velocity $u = u_0 \cos(nt)$ in the same direction cause nanofluid flow inside the channel. The channel's walls are kept at the same temperature T_0. The configuration of the current issue is exhibited in Fig. 1. All physical factors, apart from pressure, rely only on y and t because the channel walls have immeasurable extent in $x-$ and $z-$ directions and the movement is fully elaborated. It is expected that the nanopaticles will be uniformly shaped and sized. The dimensional superintending expressions can be displayed as follows considering these statements, the benchmark Boussinesq's reincarnation, and the nanofluid design (See, Swain et al. [2] and Venkateswarlu et al. [4]).

Continuity equation:

$$\frac{\partial v}{\partial y}=0 \tag{1}$$

Momentum conservation equations:

$$\frac{\partial u}{\partial t}+V_0\frac{\partial u}{\partial y}+2\Omega\omega=-\frac{1}{\rho_{nf}}\frac{\partial p}{\partial x}+\frac{\mu_{nf}}{\rho_{nf}}\frac{\partial^2 u}{\partial y^2}-\frac{\sigma_{nf}B_0^2}{\rho_{nf}}\left[\frac{u+mw}{1+m^2}\right]+g\beta_{nf}\left(T-T_0\right)+g\beta_{nf}\left(C-C_0\right)-\frac{\mu_{nf}}{\rho_{nf}}\frac{u}{k_p} \tag{2}$$

$$\frac{\partial w}{\partial t}+V_0\frac{\partial w}{\partial y}-2\Omega u=-\frac{1}{\rho_{nf}}\frac{\partial p}{\partial z}+\frac{\mu_{nf}}{\rho_{nf}}\frac{\partial^2 w}{\partial y^2}+\frac{\sigma_{nf}B_0^2}{\rho_{nf}}\left[\frac{mu-w}{1+m^2}\right]-\frac{\mu_{nf}}{\rho_{nf}}\frac{w}{k_p} \tag{3}$$

Energy conservation equation:

$$\frac{\partial T}{\partial t}+V_0\frac{\partial T}{\partial y}=\frac{k_{nf}}{\left(\rho c_p\right)_{nf}}\frac{\partial^2 T}{\partial y^2}+\frac{Q_0\left(T-T_0\right)}{\left(\rho c_p\right)_{nf}} \tag{4}$$

Mass conservation equation:

$$\frac{\partial C}{\partial t}+V_0\frac{\partial C}{\partial y}=D_{nf}\frac{\partial^2 C}{\partial y^2}+\frac{D_m k_{nf}}{T_m}\frac{\partial^2 T}{\partial y^2} \tag{5}$$

The momentum and energy equation’s initial and boundary conditions are listed below.

$$\left.\begin{array}{l} u=u_0\cos(nt), w=0, T=T_1+\varepsilon\left(T_1-T_0\right)\exp(int), C=C_1+\varepsilon\left(C_1-C_0\right)\exp(int) \text{ at } y=a \\ u=0,\quad w=0,\quad T=T_0\quad C=C_0\quad \text{at}\quad y=0 \end{array}\right\} \tag{6}$$

We take the pressure gradient components $\frac{1}{\rho_{nf}}\frac{\partial p}{\partial x}$ and $\frac{1}{\rho_{nf}}\frac{\partial p}{\partial z}$ in the following way for a purely oscillatory flow (See, Venkateswarlu et al. [4]).

$$\frac{1}{\rho_{nf}}\frac{\partial p}{\partial x}=-\frac{\sigma_{nf}B_0^2 m u_0}{\rho_{nf}\left(1+m^2\right)} \tag{7}$$

$$\frac{1}{\rho_{nf}}\frac{\partial p}{\partial z}=2\Omega u_0+\frac{\sigma_{nf}B_0^2 m u_0}{\rho_{nf}\left(1+m^2\right)} \tag{8}$$

By replacing Eqs. (2) and (3) with Eqs. (7) and (8), we derived

$$\frac{\partial u}{\partial t}+V_0\frac{\partial u}{\partial y}+2\Omega\omega=\frac{\mu_{nf}}{\rho_{nf}}\frac{\partial^2 u}{\partial y^2}-\frac{\sigma_{nf}B_0^2}{\rho_{nf}}\left[\frac{u+mw-u_0}{1+m^2}\right]+g\beta_{nf}\left(T-T_0\right)+g\beta_{nf}\left(C-C_0\right)-\frac{\mu_{nf}}{\rho_{nf}}\frac{u}{k_p} \tag{9}$$

$$\frac{\partial w}{\partial t}+V_0\frac{\partial w}{\partial y}-2\Omega\left(u-u_0\right)=\frac{\mu_{nf}}{\rho_{nf}}\frac{\partial^2 w}{\partial y^2}-\frac{\sigma_{nf}B_0^2}{\rho_{nf}}\left[\frac{mu_0+w-mu}{1+m^2}\right]-\frac{\mu_{nf}}{\rho_{nf}}\frac{w}{k_p} \tag{10}$$

For spherical nanoparticles, μ_{nf} , ρ_{nf} , $\left(\rho c_p\right)_{nf}$,and $(\rho\beta)_{nf}$ can be interpreted as

$$\mu_{nf}=\frac{\mu_f}{(1-\chi)^{2.5}} \tag{11}$$

$$\rho_{nf}=(1-\chi)\rho_f+\chi\rho_s \tag{12}$$

$$\left(\rho c_p\right)_{nf}=(1-\chi)\left(\rho c_p\right)_f+\chi\left(\rho c_p\right)_s \tag{13}$$

$$(\rho\beta)_{nf}=(1-\chi)(\rho\beta)_f+\chi(\rho\beta)_s \tag{14}$$

Expressions for the nanoliquid's existing thermal conductivity and electrical conductivity are

$$\frac{k_{nf}}{k_f}=\frac{\left(k_s+2k_f\right)-2\chi\left(k_f-k_s\right)}{\left(k_s+2k_f\right)+\chi\left(k_f-k_s\right)} \tag{15}$$

$$\frac{\sigma_{nf}}{\sigma_f}=1+\frac{3\chi\left(\sigma_s-\sigma_f\right)}{\left(\sigma_s+2\sigma_f\right)-\chi\left(\sigma_s-\sigma_f\right)} \tag{16}$$

Table 1. Thermo-physical specifications of TiO_2 nanoparticles and kerosene oil (See, Abbas et al. [32])

Property	TiO_2	Kerosene Oil
$k\ (W/mK)$	8.953	0.15
$\rho\ (Kg/m^3)$	4250	783
$c_p\ (J/Kg\,K)$	686.2	2090
$\sigma(S/m)$	2.6×10^{6}	5×10^{-11}
$\beta\ (K^{-1})$	0.9×10^{-5}	99×10^{-5}

The subsequent non-dimensional values are displayed

$$\left. U=\frac{a\rho_f}{\mu_f}u, W=\frac{a\rho_f}{\mu_f}w, \theta=\frac{T-T_0}{T_1-T_0}, \eta=\frac{y}{a}, \omega=\frac{a^2\rho_f}{\mu_f}n,\ \ \tau=\frac{\mu_f}{a^2\rho_f}t,\ \ \phi=\frac{C-C_0}{C_1-C_0}, \right\} \tag{17}$$

Eqs. (4), (5), (9) and (10) are used to produce the displayed non-dimensional structure

$$\frac{\partial U}{\partial\tau}+s\frac{\partial U}{\partial\eta}+2K^2W=a_6\frac{\partial^2U}{\partial\eta^2}-a_7M\left[\frac{U+mW-\lambda}{1+m^2}\right]+a_4Gr\theta+a_5Gm\phi-\frac{a_6}{Da}U \tag{18}$$

$$\frac{\partial W}{\partial\tau}+s\frac{\partial W}{\partial\eta}-2K^2\left(U-\lambda\right)=a_6\frac{\partial^2W}{\partial\eta^2}-a_7M\left[\frac{m\lambda+W-mU}{1+m^2}\right]-\frac{a_6}{Da}W \tag{19}$$

$$\frac{\partial\theta}{\partial\tau}+s\frac{\partial\theta}{\partial\eta}=\frac{a_{10}}{\Pr}\frac{\partial^2\theta}{\partial\eta^2}+\frac{H}{a_9}\theta \tag{20}$$

$$\frac{\partial\phi}{\partial\tau}+s\frac{\partial\phi}{\partial\eta}=\frac{1}{Sc}\frac{\partial^2\phi}{\partial\eta^2}+a_8Sr\frac{\partial^2\theta}{\partial\eta^2} \tag{21}$$

Here

$$s=\frac{V_0a}{\nu_f}, K^2=\frac{2\Omega a^2}{\nu_f}, Gr=\frac{g\left(\rho\beta\right)_f\left(T_1-T_0\right)a^3}{\nu_f^2}, M=\frac{\sigma_fB_0^2a^2}{\rho_f\nu_f}, \lambda=\frac{u_0a}{\nu_f}, Sc=\frac{\nu_f}{D_m},\ \Pr=\frac{\left(\rho c_p\right)_f\nu_f}{k_f},\ H=\frac{Q_0a^2}{\nu_f\left(\rho c_p\right)_f},$$

$$Da=\frac{k_p}{a^2}, Gm=\frac{g\left(\rho\beta\right)_f\left(C_1-C_0\right)a^3}{\nu_f^2}, Sr=\frac{D_m\left(T_1-T_0\right)k_f}{T_m\left(C_1-C_0\right)\nu_f}.$$

For a non-dimensional structure, the initial and boundary conditions are as follows:

$$\left.\begin{array}{l} U=0,\ W=0,\ \theta=0,\ \phi=0 \text{ at } \eta=0 \\ U=\lambda\cos\left(\omega\tau\right), W=0,\ \theta=1+\varepsilon\exp\left(i\omega\tau\right), \phi=1+\varepsilon\exp\left(i\omega\tau\right) \text{ at } \eta=1 \end{array}\right\} \tag{22}$$

Define:

$$\psi=U+iW \tag{23}$$

By utilizing Eq. (23) in Eqs. (18) and (19), we acquired

$$\frac{\partial\psi}{\partial\tau}+s\frac{\partial\psi}{\partial\eta}-2iK^2\left(\psi-\lambda\right)=a_6\frac{\partial^2\psi}{\partial\eta^2}-a_7M\left[\frac{\psi-\lambda}{1+im}\right]+a_4Gr\theta+a_5Gm\phi-\frac{a_6}{Da}\psi \tag{24}$$

The initial and boundary conditions can be translated into the structure

$$\left.\begin{array}{l} \psi=0,\ \theta=0,\ \phi=0 \text{ at } \eta=0 \\ \psi=\lambda\cos\left(\omega\tau\right), \theta=1+\varepsilon\exp\left(i\omega\tau\right), \phi=1+\varepsilon\exp\left(i\omega\tau\right) \text{ at } \eta=1 \end{array}\right\} \tag{25}$$

The shear stress τ_w, heat flux q_w and mass flux j_w are acquired utilizing the nanoliquid velocity, temperature, and concentration as

$$\tau_w = \mu_{nf}\left[\frac{\partial u}{\partial y} + i\frac{\partial w}{\partial y}\right] \tag{26}$$

$$q_w = -k_{nf}\left[\frac{\partial T}{\partial y}\right] \tag{27}$$

$$j_w = -D_m\left[\frac{\partial C}{\partial y}\right] \tag{28}$$

The skin-friction coefficient Cf, heat transfer coefficient Nu and mass transfer coefficient Sh in a non-dimensional pattern can be represented as

$$Cf = \frac{a^2 \tau_w \rho_{nf}}{\mu_{nf}^2} \tag{29}$$

$$Nu = \frac{a q_w}{k_{nf}\left(T_1 - T_0\right)} \tag{30}$$

$$Sh = \frac{a\, j_w}{D_m\left(C_1 - C_0\right)} \tag{31}$$

We calculated the physical parameters by replacing Eqs. (26) to (28) in Eqs. (29) to (31)

$$Cf = a_{11}\left[\frac{\partial \psi}{\partial \eta}\right] \tag{32}$$

$$Nu = -\left[\frac{\partial \theta}{\partial \eta}\right] \tag{33}$$

$$Sh = -\left[\frac{\partial \phi}{\partial \eta}\right] \tag{34}$$

3. THE PROBLEM'S SOLUTION

It is impossible to solve the corresponding non-linear partial differential equations (18) to (21) in closed form. These non-linear partial differential equations are thus reduced to a set of ordinary differential equations that may be solved analytically. This can be achieved by using the trial solutions as shown below (See, Venkateswarlu et al. [4])

$$\psi(\eta,\tau) = \psi_0(\eta) + \varepsilon \exp\left(i\,\omega\tau\right)\psi_1(\eta) + O\left(\varepsilon^2\right) \tag{35}$$

$$\theta(\eta,\tau) = \theta_0(\eta) + \varepsilon \exp\left(i\,\omega\tau\right)\theta_1(\eta) + O\left(\varepsilon^2\right) \tag{36}$$

$$\phi(\eta,\tau) = \phi_0(\eta) + \varepsilon \exp\left(i\,\omega\tau\right)\phi_1(\eta) + O\left(\varepsilon^2\right) \tag{37}$$

The subsequent ordinary differential equations can be obtained by substituting Eqs. (35) to (37) into Eqs. (18) to (21)

$$a_6\frac{d^2\psi_0}{d\eta^2} - s\frac{d\psi_0}{d\eta} - \left[\frac{a_7 M}{1+im} + \frac{a_6}{Da} - 2iK^2\right]\psi_0 = -\left[a_4 Gr\theta_0 + a_5 Gm\phi_0 + \left(\frac{a_7 M}{1+im} - 2iK^2\right)\lambda\right] \tag{38}$$

$$a_6\frac{d^2\psi_1}{d\eta^2} - s\frac{d\psi_1}{d\eta} - \left[\frac{a_7 M}{1+im} + \frac{a_6}{Da} - 2iK^2 + i\omega\right]\psi_1 = -\left[a_4 Gr\theta_1 + a_5 Gm\phi_1\right] \tag{39}$$

$$\frac{a_{10}}{Pr}\frac{d^2\theta_0}{d\eta^2} - s\frac{d\theta_0}{d\eta} + \frac{H}{a_9}\theta_0 = 0 \tag{40}$$

$$\frac{a_{10}}{Pr}\frac{d^2\theta_1}{d\eta^2}-s\frac{d\theta_1}{d\eta}+\left(\frac{H}{a_9}-i\,\omega\right)\theta_1=0 \tag{41}$$

$$\frac{1}{Sc}\frac{d^2\phi_0}{d\eta^2}-s\frac{d\phi_0}{d\eta}=-a_8\,Sr\frac{d^2\theta_0}{d\eta^2} \tag{42}$$

$$\frac{1}{Sc}\frac{d^2\phi_1}{d\eta^2}-s\frac{d\phi_1}{d\eta}-i\,\omega\phi_1=-a_8\,Sr\frac{d^2\theta_1}{d\eta^2} \tag{43}$$

The pertinent initial and boundary conditions can be characterized as

$$\left.\begin{array}{l}\psi_0=0,\,\psi_1=0,\,\theta_0=0,\,\theta_1=0\phi_o=0,\,\phi_1=0\quad\text{at}\quad\eta=0\\ \psi_0=\lambda\cos(\omega\tau),\,\psi_1=0,\,\theta_0=1,\,\theta_1=1,\,\phi_0=1,\,\phi_1=1\ \text{at}\quad\eta=1\end{array}\right\} \tag{44}$$

Eqs. (38) to (43) with the boundary conditions in Eqs. (44) have analytical solutions that are provided by

$$\psi_0=a_{49}\exp(m_8\eta)+a_{50}\exp(m_9\eta)-a_{41}\exp(m_1\eta)+a_{42}\exp(m_2\eta)-a_{43}\exp(-m_5\eta)-a_{44}\exp(m_5\eta)+a_{45} \tag{45}$$

$$\psi_1=a_{60}\exp(m_{10}\eta)+a_{61}\exp(m_{11}\eta)-a_{53}\exp(m_3\eta)+a_{54}\exp(m_4\eta)-a_{55}\exp(m_6\eta)-a_{56}\exp(m_7\eta) \tag{46}$$

$$\theta_0=a_{17}\left[\exp(m_1\eta)-\exp(m_2\eta)\right] \tag{47}$$

$$\theta_1=a_{17}\left[\exp(m_3\eta)-\exp(m_4\eta)\right] \tag{48}$$

$$\phi_0=a_{26}\exp(-m_5\eta)+a_{21}\exp(m_5\eta)-a_{24}\exp(m_1\eta)+a_{25}\exp(m_2\eta) \tag{49}$$

$$\phi_1=a_{36}\exp(m_6\eta)+a_{35}\exp(m_7\eta)-a_{30}\exp(m_3\eta)+a_{31}\exp(m_4\eta) \tag{50}$$

We found the following solutions for the nanofluid velocity, temperature, and concentration by replacing Eqs. (35) to (37) with Eqs. (45) to (50)

$$\begin{array}{l}\psi(\eta,\tau)=\begin{bmatrix}a_{49}\exp(m_8\eta)+a_{50}\exp(m_9\eta)-a_{41}\exp(m_1\eta)+\\ a_{42}\exp(m_2\eta)-a_{43}\exp(-m_5\eta)-a_{44}\exp(m_5\eta)+a_{45}\end{bmatrix}+\\ \varepsilon\exp(i\omega\tau)\begin{bmatrix}a_{60}\exp(m_{10}\eta)+a_{61}\exp(m_{11}\eta)-a_{53}\exp(m_3\eta)+\\ a_{54}\exp(m_4\eta)-a_{55}\exp(m_6\eta)-a_{56}\exp(m_7\eta)\end{bmatrix}\end{array} \tag{51}$$

$$\theta(\eta,\tau)=a_{17}\left[\exp(m_1\eta)-\exp(m_2\eta)\right]+\varepsilon\exp(i\omega\tau)a_{17}\left[\exp(m_3\eta)-\exp(m_4\eta)\right] \tag{52}$$

$$\begin{array}{l}\phi(\eta,\tau)=\left[a_{26}\exp(-m_5\eta)+a_{21}\exp(m_5\eta)-a_{24}\exp(m_1\eta)+a_{25}\exp(m_2\eta)\right]+\\ \varepsilon\exp(i\omega\tau)\left[a_{36}\exp(m_6\eta)+a_{35}\exp(m_7\eta)-a_{30}\exp(m_3\eta)+a_{31}\exp(m_4\eta)\right]\end{array} \tag{53}$$

3.1 Skin friction coefficient

The velocity field can be utilized to express the skin friction coefficient as

$$\begin{array}{l}Cf=\begin{bmatrix}a_{49}m_8\exp(m_8\eta)+a_{50}m_9\exp(m_9\eta)-a_{41}m_1\exp(m_1\eta)+\\ a_{42}m_2\exp(m_2\eta)+a_{43}m_5\exp(-m_5\eta)-a_{44}m_5\exp(m_5\eta)\end{bmatrix}+\\ \varepsilon\exp(i\omega\tau)\begin{bmatrix}a_{60}m_{10}\exp(m_{10}\eta)+a_{61}m_{11}\exp(m_{11}\eta)-a_{53}m_3\exp(m_3\eta)+\\ a_{54}m_4\exp(m_4\eta)-a_{55}m_6\exp(m_6\eta)-a_{56}m_7\exp(m_7\eta)\end{bmatrix}\end{array} \tag{54}$$

$$Pcf=\text{Real part of }(Cf) \tag{55}$$

$$Scf=\text{Imaginary part of}(Cf) \tag{56}$$

3.2 Heat transfer coefficient

The temperature field can be utilized to express the heat transfer coefficient as

$$Nu = a_{17}\left[m_1 \exp(m_1\eta) - m_2 \exp(m_2\eta)\right] + \varepsilon \exp(i\omega\tau) a_{17}\left[m_3 \exp(m_3\eta) - m_4 \exp(m_4\eta)\right] \tag{57}$$

3.3 Mass transfer coefficient

The concentration field can be utilized to express the mass transfer coefficient as

$$\begin{aligned} Sh = &\left[a_{21}m_5 \exp(m_5\eta) - a_{26}m_5 \exp(-m_5\eta) - a_{24}m_1 \exp(m_1\eta) + a_{25}m_2 \exp(m_2\eta)\right] + \\ &\varepsilon \exp(i\omega\tau)\left[a_{36}m_6 \exp(m_6\eta) + a_{35}m_7 \exp(m_7\eta) - a_{30}m_3 \exp(m_3\eta) + a_{31}m_4 \exp(m_4\eta)\right] \end{aligned} \tag{58}$$

4. FINDINGS AND DISCUSSION

To memorize the implications of distinct parameters, such as the rotation factor K^2, magnetic parameter M, upper wall motion parameter λ, thermal Grashof number Gr, solutal Grashof number Gm, Darcy parameter Da, Hall current parameter m, Soret number Sr, heat generation factor H, suction factor s, and solid volume fraction χ on the flow configuration, the numerical assessments of the titanium dioxide nanoliquid primary velocity U, secondary velocity W, temperature θ, concentration ϕ, primary skin friction Pcf, secondary skin friction Scf, heat transfer coefficient Nu, and mass transfer coefficient Nu are computed. The subsequent parameter values are utilized for numerical calculations in this study: $\chi = 0.05$, $K^2 = 1$, $M = 1$, $s = 2$, $\lambda = 0.001$, $Gr = 1$, $Gm = 1$, $Da = 1$, $m = 1$, $\Pr = 0.71$, $Sr = 5$, $H = 2$, $Sc = 0.22$, and $\tau = \pi/2$.The velocity profile data depict the primary velocity of titanium dioxide-kerosene nanoliquid as a solid line and the secondary velocity as a dashed line. To obtain the numerical findings of the current work, a MATLAB (2015a) program was established. To compare our results with those of Ref [4] as a special case, we calculated the numerical values of primary and secondary skin friction coefficients for our work as well as those of Ref [4] which is displayed in Tables 2 and 3. There is a significant level of agreement between the two findings.

Table 2. Comparison of primary skin friction coefficient Pcf with Ref [4] when $\tau = \pi/2$, $K^2 = m = Da = \Pr = \omega = 1$, $Sc = 0.6$, $\lambda = 0.001$, $Gr = 2$, $Gm = 4$, $Sr = 5$, $H = -1$, $s = 0$ and $\chi = 0$.

η	M	Pcf		M	Pcf		M	Pcf	
		Ref [4]	Present		Ref [4]	Present		Ref [4]	Present
0.00	1.0	0.2221	0.2222	2.0	0.2068	0.2069	3.0	0.1928	0.0928
0.25	1.0	0.1936	0.1937	2.0	0.1820	0.1821	3.0	0.1713	0.1714
0.50	1.0	0.0907	0.0907	2.0	0.0893	0.0893	3.0	0.0878	0.0879
0.75	1.0	-0.1417	-0.1416	2.0	-0.1303	-0.1302	3.0	-0.1198	-0.1197
1.00	1.0	-0.6018	-0.6017	2.0	-0.5832	-0.5831	3.0	-0.5658	-0.5657

Table 3. Comparison of secondary skin friction coefficient Pcf with Ref [4] when $\tau = \pi/2$, $K^2 = m = Da = \Pr = \omega = 1$, $Sc = 0.6$, $\lambda = 0.001$, $Gr = 2$, $Gm = 4$, $Sr = 5$, $H = -1$, $s = 0$ and $\chi = 0$.

η	M	Scf		M	Scf		M	Scf	
		Ref [4]	Present		Ref [4]	Present		Ref [4]	Present
0.00	1.0	0.0593	0.0593	2.0	0.0638	0.0638	3.0	0.0670	0.0670
0.25	1.0	0.0456	0.0456	2.0	0.0494	0.0494	3.0	0.0522	0.0522
0.50	1.0	0.0066	0.0066	2.0	0.0077	0.0077	3.0	0.0087	0.0087
0.75	1.0	-0.0446	-0.0445	2.0	-0.0482	-0.0481	3.0	-0.0508	-0.0507
1.00	1.0	-0.0750	-0.0749	2.0	-0.0821	-0.0820	3.0	-0.0877	-0.0876

Figs. 2, 3, and 4 are displayed to explore the implications of λ, K^2 and H on U and W respectively. It is detected that U minimizes and W maximizes with an elevation in λ, K^2 and H .The secondary movement is directed by the Coriolis force and is generated by the motion of the upper wall. Driven by the Coriolis force, a stronger secondary flow forms as the upper wall moves faster. This secondary flow slows down the primary flow due to viscous and inertial factors. Due to the Coriolis force that opposes the primary flow and drives a secondary circulation, the growing rotation parameter in MHD nanofluid flow reduces the primary velocity and increases the secondary velocity. Acting perpendicular to the direction of motion and rotation, the Coriolis force acts as a fictitious force. Increasing the heat generation parameter makes the fluid less dense and less susceptible to the magnetic field's braking effect, thereby reducing the primary velocity while increasing the secondary velocity due to heat generation, creating a secondary flow.

Primary and secondary velocity profiles across a range of magnetic parameters and thermal Grashof numbers are shown in Figs. 5 and 6. The primary and secondary velocity profiles are observed to decrease as the magnetic factor and the thermal Grashof number increase. The magnetic parameter quantifies the strength of the Lorentz force relative to the fluid's viscous or inertial forces. Increased frictional resistance along the plate's surface may result from a stronger magnetic field, which could lower both primary and secondary velocities. The thermal Grashof number is defined as the ratio of buoyancy forces to viscous forces acting on a nanofluid. Primary and secondary velocity profiles have inverse relation with thermal Grashof number because of high degree of kinematic viscosity of the titanium dioxide nanofluid. The significance of the Soret number on the primary and secondary velocity profiles for titanium dioxide nanofluid based on kerosene is described in Fig. 7. Soret parameter measures the contribution of a temperature gradient to mass diffusion, which typically results in the separation of different chemical species or solutes within a nanofluid mixture. The primary and secondary velocity profiles diminish as the Soret number expands, indicating that additional heat input causes the nanofluid's velocity to slow down.

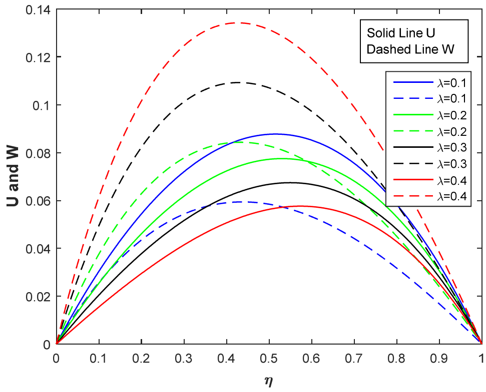

Figure 2. Variation of U and W in reference to λ

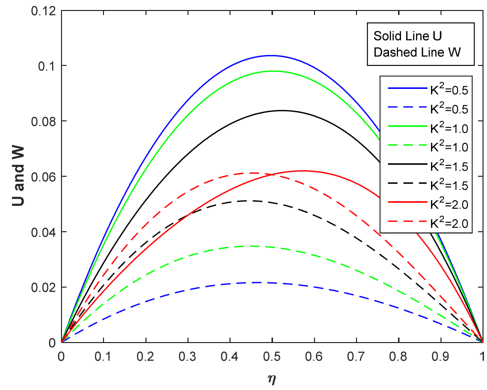

Figure 3. Variation of U and W in reference to K^2

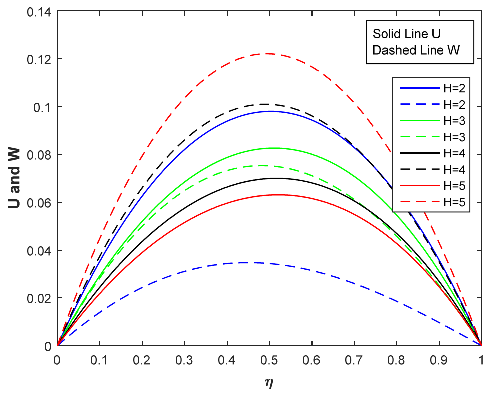

Figure 4. Variation of U and W in reference to H

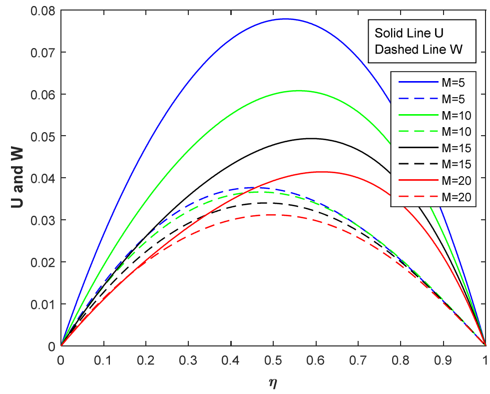

Figure 5. Variation of U and W in reference to M

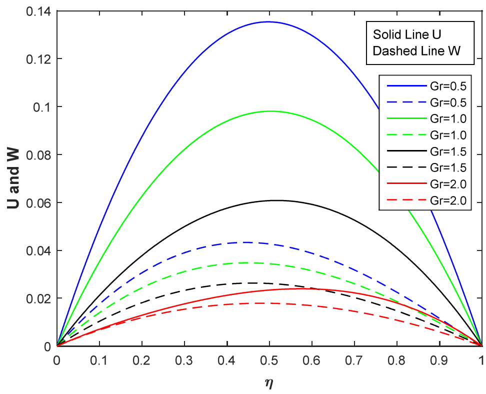

Figure 6. Variation of U and W in reference to Gr

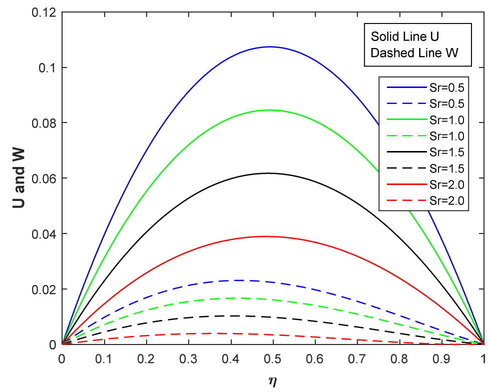

Figure 7. Variation of U and W in reference to Sr

The implications of the solutal Grashof number, Darcy parameter, and Hall current parameter on the primary and secondary velocity profiles are displayed in Figs. 8, 9, and 10. Instead of temperature, the mass Grashof number controls the behavior of natural convection caused by concentration or density gradients of a dissolved substance. The primary and secondary velocity profiles of the kerosene-based titanium dioxide nanofluid improve as one increases the solutal Grashof number, Darcy parameter, and Hall current. The nanofluid's kinematic and thermal effects, which might have an impact on the total velocity distribution, are also influenced by the Darcy parameter. Higher Darcy parameters can result in better primary and secondary velocity profiles and more effective heat transfer. Increasing the Hall current parameter directly enhances both primary and secondary velocity profiles because of the changed momentum distribution.

Figs. 11 and 12 display the primary and secondary velocity profiles for varies values of Schmidt number and Prandtl number. The Schmidt number establishes whether the momentum of a nanofluid is transported more quickly or more slowly than the dissolved mass. The relative thickness of a fluid's velocity and thermal boundary layers are directly determined by the Prandtl number, which assesses whether a fluid's momentum or heat spreads more quickly. As both parameters go up, the primary and secondary velocity profiles also become greater. The Reynolds number, a measurement of the fluid's viscosity and inertia, is directly correlated with the Schmidt number. The velocity profiles increased due to greater inertia and viscosity resulting from a higher Reynolds number, as indicated by an elevated Schmidt number. A fluid with a higher Prandtl number can move more easily and have less flow resistance because its viscosity is significantly lower than its thermal diffusivity. Primary and secondary velocities rise as a result.

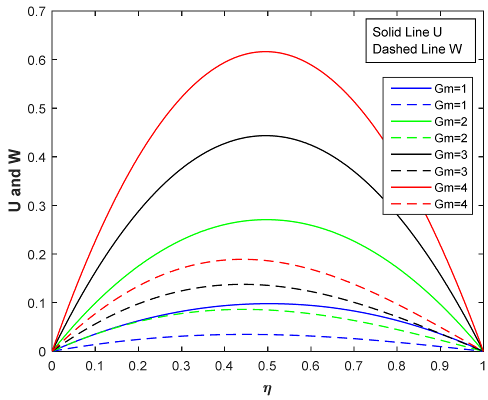

Figure 8. Variation of U and W in reference to Gm

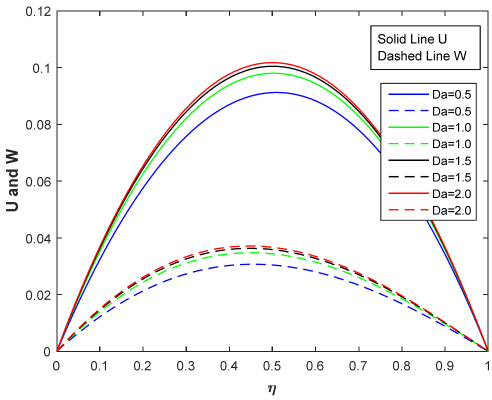

Figure 9. Variation of U and W in reference to Da

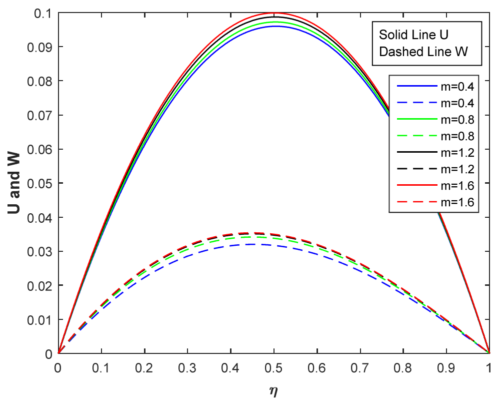

Figure 10. Variation of U and W in reference to m

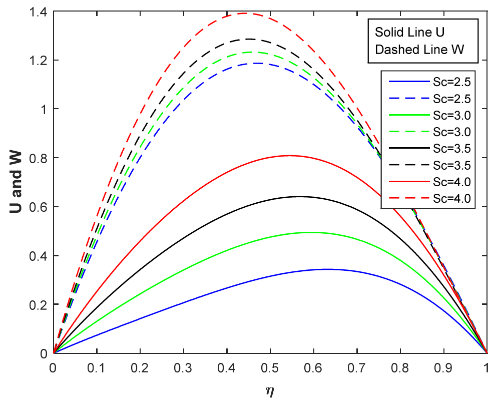

Figure 11. Variation of U and W in reference to Sc

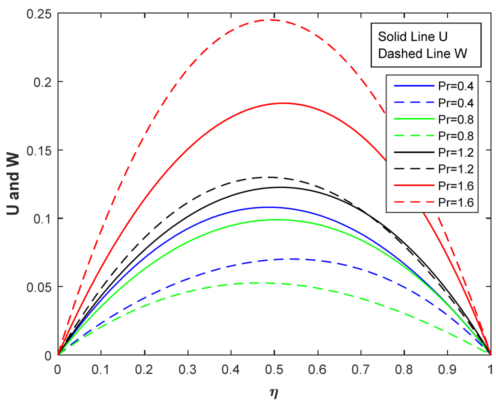

Figure 12. Variation of U and W in reference to Pr

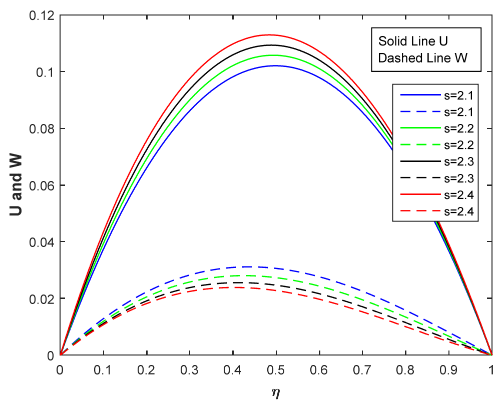

Figure 13. Variation of U and W in reference to s

Figs. 13 and 14 show the rise in primary velocity and reduction in secondary velocity of a titanium dioxide nanofluid whenever the suction parameter and volume fraction parameter grow. The physical impact of withdrawing fluid through a porous surface or slot is measured using the suction parameter. Nanofluids may expand because of the volume fraction rise, which could raise the fluid's primary velocity. The magnetic field can influence flow characteristics. Increasing the volume fraction parameter may promote a more uniform distribution of the fluid, potentially leading to enhanced primary velocity. The volume of suspended nanoparticles divided by the entire volume of the nanofluid mixture is the volume fraction parameter.

Figs. 15–18 analyze how factors such as the heat generation parameter, Prandtl number, suction parameter, and volume fraction parameter influence the temperature domain. It is evident that the temperature domain grows with rises in the heat generation parameter, Prandtl number, and suction parameter. The temperature profile lowers as the volume fraction parameter rises. Both the amount and shape of titanium dioxide nanoparticles affect the thermal execution of nanofluids, leading to improved heat transfer and a more consistent temperature distribution. A higher Prandtl number suggests that the thermal boundary layer is thicker, resulting in an increased fluid temperature.

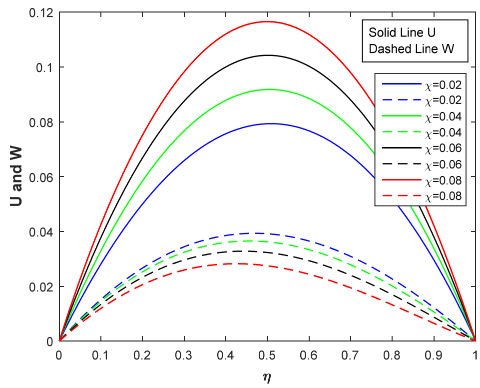

Figure 14. Variation of U and W in reference to χ

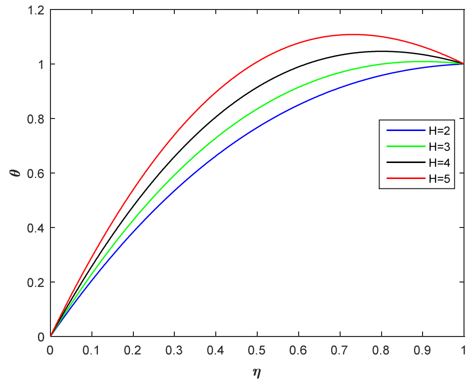

Figure 15. Variation of θ in reference to H

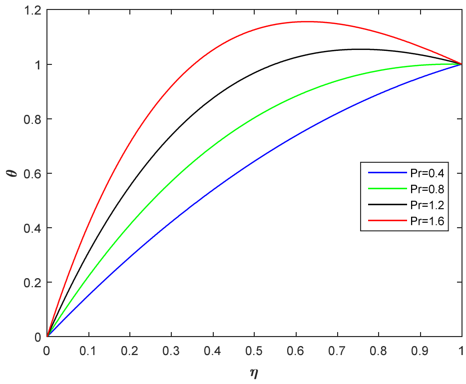

Figure 16. Variation of θ in reference to Pr

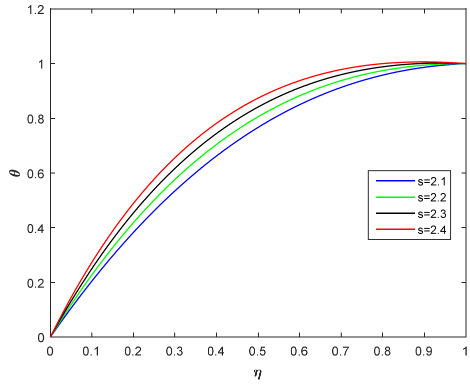

Figure 17. Variation of θ in reference to s

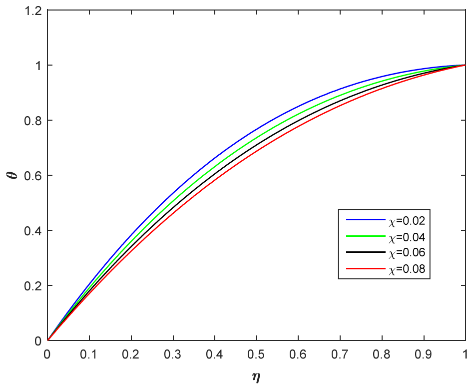

Figure 18. Variation of θ in reference to χ

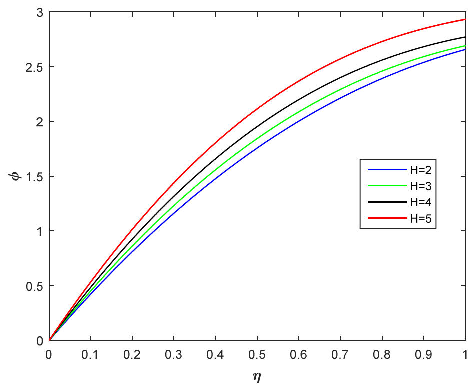

Figure 19. Variation of ϕ in reference to H

Figs. 19-23, illustrate how the concentration profile changes with varying heat generation parameter, suction parameter, Soret number, Schmidt number, and volume fraction parameter. The data demonstrate that higher values of the heat generation parameter, suction parameter, Soret number, Schmidt number, and volume fraction parameter increase mass concentration. The condensation action increases the nanofluid concentration as the suction parameter rises, thereby increasing the concentration in the flow field. Shear stress is crucial in engineering and often demands complex design solutions. A comprehensive understanding of this coefficient will lead to the development of designs for medicine delivery for cancer patients, bridges, dams, and storage efficiency.

Tables 4 through 16 show that when the upper wall motion factor, rotation parameter, magnetic parameter, Grashof number, heat generation parameter, and Schmidt number increase, the primary skin friction coefficient intensifies at the left wall and decreases at the right wall. Similarly, as the thermal Grashof number, Darcy number, Hall current parameter, Soret number, suction factor, and volume fraction factor increases, the primary skin friction coefficient decreases on the left wall and increases on the right wall. When the upper wall motion parameter, rotation parameter, thermal Grashof number, Darcy number, Hall current parameter, Soret number, and heat generation parameter are augmented, the secondary skin friction coefficient reduces at the left wall and intensifies at the right wall. Similarly, as the magnetic parameter, thermal Grashof number, Schmidt number, suction parameter, and volume fraction parameter increase, the secondary skin friction coefficient increases at the left wall and decreases at the right wall.

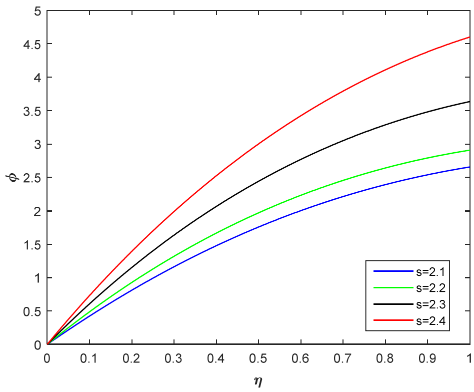

Figure 20. Variation of ϕ in reference to s

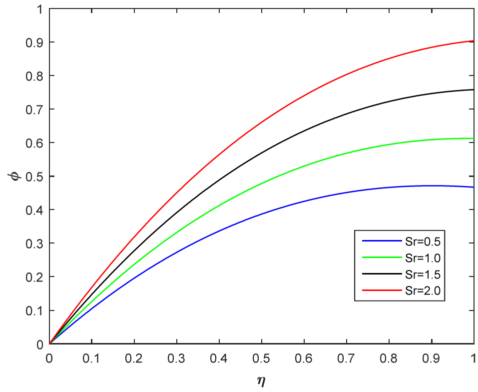

Figure 21. Variation of ϕ in reference to s

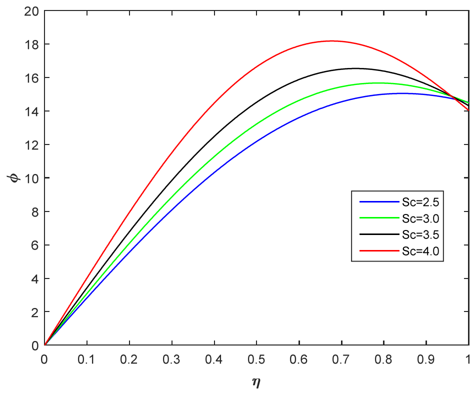

Figure 22. Variation of ϕ in reference to Sc

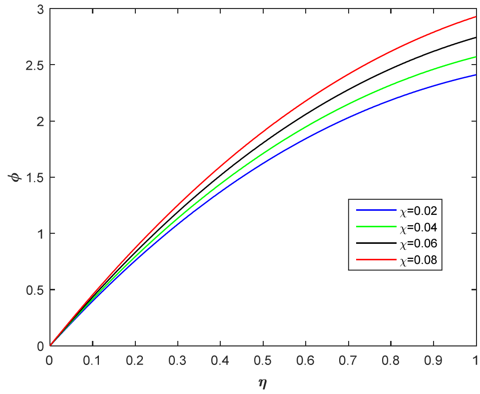

Figure 23. Variation of ϕ in reference to χ

Table 4. Interpretation of Pcf and Scf with respect to λ

η	λ	Pcf	Scf	λ	Pcf	Scf	λ	Pcf	Scf
0.00	0.1	-0.3373	-0.3010	0.2	-0.2789	-0.4463	0.3	-0.2206	-0.5916
0.25	0.1	-0.1763	-0.1078	0.2	-0.1575	-0.1484	0.3	-0.1387	-0.1891
0.50	0.1	-0.0106	0.0303	0.2	-0.0189	0.0454	0.3	-0.0272	0.0606
0.75	0.1	0.1723	0.1241	0.2	0.1496	0.1740	0.3	0.1269	0.2239
1.00	0.1	0.3731	0.1744	0.2	0.3468	0.2512	0.3	0.3206	0.3280

Table 5. Interpretation of Pcf and Scf with respect to K^2

η	K^2	Pcf	Scf	K^2	Pcf	Scf	K^2	Pcf	Scf
0.00	0.5	-0.4236	-0.0945	1.0	-0.3951	-0.1572	1.5	-0.3212	-0.2331
0.25	0.5	-0.2057	-0.0424	1.0	-0.1949	-0.0675	1.5	-0.1669	-0.0991
0.50	0.5	0.0026	0.0063	1.0	-0.0024	0.0153	1.5	-0.0153	0.0248
0.75	0.5	0.2076	0.0453	1.0	0.1948	0.0747	1.5	0.1618	0.1114
1.00	0.5	0.4103	0.0703	1.0	0.3991	0.0984	1.5	0.3706	0.1350

Table 6. Interpretation of Pcf and Scf with respect to M

η	M	Pcf	Scf	M	Pcf	Scf	M	Pcf	Scf
0.00	5	-0.2956	-0.1681	10	-0.2122	-0.1591	15	-0.1579	-0.1431
0.25	5	-0.1550	-0.0736	10	-0.1202	-0.0722	15	-0.0963	-0.0675
0.50	5	-0.0169	0.0146	10	-0.0273	0.0101	15	-0.0325	0.0051
0.75	5	0.1483	0.0814	10	0.1079	0.0791	15	0.0804	0.0732
1.00	5	0.3551	0.1077	10	0.3148	0.1100	15	0.2854	0.1084

Table 7. Interpretation of Pcf and Scf with respect to Gr

η	Gr	Pcf	Scf	Gr	Pcf	Scf	Gr	Pcf	Scf
0.00	0.5	-0.5535	-0.1980	1.0	-0.3951	-0.1572	1.5	-0.2366	-0.1164
0.25	0.5	-0.2686	-0.0836	1.0	-0.1949	-0.0675	1.5	-0.1211	-0.0514
0.50	0.5	0.0034	0.0216	1.0	-0.0024	0.0153	1.5	-0.0081	0.0090
0.75	0.5	0.2712	0.0935	1.0	0.1948	0.0747	1.5	0.1185	0.0558
1.00	0.5	0.5357	0.1158	1.0	0.3991	0.0984	1.5	0.2626	0.0810

Table 8. Interpretation of Pcf and Scf with respect to Gm

η	Gm	Pcf	Scf	Gm	Pcf	Scf	Gm	Pcf	Scf
0.00	1.0	-0.3951	-0.1572	2.0	-1.1076	-0.3945	3.0	-1.8202	-0.6318
0.25	1.0	-0.1949	-0.0675	2.0	-0.5374	-0.1669	3.0	-0.8799	-0.2662
0.50	1.0	-0.0024	0.0153	2.0	0.0068	0.0431	3.0	0.0161	0.0709
0.75	1.0	0.1948	0.0747	2.0	0.5427	0.1866	3.0	0.8905	0.2985
1.00	1.0	0.3991	0.0984	2.0	1.0716	0.2308	3.0	1.7440	0.3632

Table 9. Interpretation of Pcf and Scf with respect to Da

η	Da	Pcf	Scf	Da	Pcf	Scf	Da	Pcf	Scf
0.00	0.5	-0.3625	-0.1371	1.0	-0.3951	-0.1572	1.5	-0.4070	-0.1649
0.25	0.5	-0.1815	-0.0599	1.0	-0.1949	-0.0675	1.5	-0.1997	-0.0704
0.50	0.5	-0.0068	0.0118	1.0	-0.0024	0.0153	1.5	-0.0007	0.0166
0.75	0.5	0.1793	0.0657	1.0	0.1948	0.0747	1.5	0.2005	0.0781
1.00	0.5	0.3841	0.0906	1.0	0.3991	0.0984	1.5	0.4046	0.1013

Table 10. Interpretation of Pcf and Scf with respect to m

η	m	Pcf	Scf	m	Pcf	Scf	m	Pcf	Scf
0.00	0.4	-0.3855	-0.1438	0.8	-0.3914	-0.1543	1.2	-0.3985	-0.1589
0.25	0.4	-0.1909	-0.0623	0.8	-0.1934	-0.0664	1.2	-0.1963	-0.0682
0.50	0.4	-0.0036	0.0132	0.8	-0.0029	0.0148	1.2	-0.0019	0.0156
0.75	0.4	0.1902	0.0686	0.8	0.1931	0.0734	1.2	0.1965	0.0755
1.00	0.4	0.3945	0.0928	0.8	0.3975	0.0972	1.2	0.4007	0.0990

Table 11. Interpretation of Pcf and Scf with respect to Sr

η	Sr	Pcf	Scf	Sr	Pcf	Scf	Sr	Pcf	Scf
0.00	0.5	0.4445	0.1104	1.0	0.3512	0.0807	1.5	0.2579	0.0510
0.25	0.5	0.2127	0.0437	1.0	0.1674	0.0314	1.5	0.1221	0.0190
0.50	0.5	-0.0068	-0.0175	1.0	-0.0063	-0.0138	1.5	-0.0058	-0.0102
0.75	0.5	-0.2163	-0.0515	1.0	-0.1706	-0.0375	1.5	-0.1249	-0.0234
1.00	0.5	-0.4163	-0.0451	1.0	-0.3257	-0.0292	1.5	-0.2351	-0.0132

Table 12. Interpretation of Pcf and Scf with respect to H

η	H	Pcf	Scf	H	Pcf	Scf	H	Pcf	Scf
0.00	2.0	-0.3951	-0.1572	3.0	-0.3273	-0.3185	4.0	-0.2735	-0.4196
0.25	2.0	-0.1949	-0.0675	3.0	-0.1645	-0.1489	4.0	-0.1394	-0.2001
0.50	2.0	-0.0024	0.0153	3.0	-0.0070	0.0112	4.0	-0.0090	0.0081
0.75	2.0	0.1948	0.0747	3.0	0.1622	0.1546	4.0	0.1360	0.2047
1.00	2.0	0.3991	0.0984	3.0	0.3497	0.2732	4.0	0.3043	0.3846

Table 13. Interpretation of Pcf and Scf with respect to Sc

η	Sc	Pcf	Scf	Sc	Pcf	Scf	Sc	Pcf	Scf
0.00	2.5	0.8019	5.1057	3.0	1.4363	5.3947	3.5	2.0618	5.7231
0.25	2.5	0.6533	2.3513	3.0	0.9773	2.4334	3.5	1.2874	2.5279
0.50	2.5	0.3898	-0.3249	3.0	0.3865	-0.4418	3.5	0.3618	-0.5706
0.75	2.5	-0.5179	-2.5284	3.0	-0.8578	-2.6614	3.5	-1.1935	-2.8095
1.00	2.5	-2.0885	-3.7393	3.0	-2.6452	-3.5950	3.5	-3.1125	-3.4565

Table 14. Interpretation of Pcf and Scf with respect to $\Pr$

η	$\Pr$	Pcf	Scf	$\Pr$	Pcf	Scf	$\Pr$	Pcf	Scf
0.00	0.4	-0.4508	0.2592	0.8	-0.3966	-0.2300	1.2	-0.4829	-0.5454
0.25	0.4	-0.2141	0.1395	0.8	-0.1968	-0.1035	1.2	-0.2438	-0.2571
0.50	0.4	0.0113	0.0210	0.8	-0.0044	0.0148	1.2	-0.0134	0.0157
0.75	0.4	0.2206	-0.1309	0.8	0.1958	0.1106	1.2	0.2386	0.2654
1.00	0.4	0.4021	-0.3345	0.8	0.4087	0.1724	1.2	0.5295	0.4805

Table 15. Interpretation of Pcf and Scf with respect to s

η	s	Pcf	Scf	s	Pcf	Scf	s	Pcf	Scf
0.00	2.1	-0.4208	-0.1460	2.2	-0.4458	-0.1363	2.3	-0.4709	-0.1288
0.25	2.1	-0.2015	-0.0595	2.2	-0.2074	-0.0525	2.3	-0.2128	-0.0468
0.50	2.1	0.0016	0.0172	2.2	0.0056	0.0189	2.3	0.0098	0.0203
0.75	2.1	0.2037	0.0675	2.2	0.2119	0.0612	2.3	0.2197	0.0561
1.00	2.1	0.4079	0.0800	2.2	0.4153	0.0642	2.3	0.4222	0.0514

Table 16. Interpretation of Pcf and Scf with respect to χ

η	χ	Pcf	Scf	χ	Pcf	Scf	χ	Pcf	Scf
0.00	0.02	-0.3128	-0.1696	0.04	-0.3676	-0.1624	0.06	-0.4224	-0.1508
0.25	0.02	-0.1584	-0.0776	0.04	-0.1827	-0.0713	0.06	-0.2070	-0.0633
0.50	0.02	-0.0055	0.0106	0.04	-0.0035	0.0138	0.06	-0.0013	0.0168
0.75	0.02	0.1566	0.0827	0.04	0.1821	0.0778	0.06	0.2076	0.0711
1.00	0.02	0.3305	0.1285	0.04	0.3763	0.1093	0.06	0.4218	0.0866

Tables 17–20 show that the volume fraction parameter diminishes the heat transfer coefficient at the left wall and enhances it at the right, however the heat generation and suction parameters exhibit the opposite pattern. Heat generation parameter and suction parameter strengthen the mass transfer coefficient at the right wall while volume fraction parameter and Soret factor minimize it at the left wall.

Table 17. Interpretation of Nu and Sh with respect to χ

η	χ	Nu	Sh	χ	Nu	Sh	χ	Nu	Sh
0.00	0.02	2.2987	-4.1303	0.04	2.2232	-4.3129	0.06	2.1540	-4.5045
0.25	0.02	1.5584	-3.2160	0.04	1.5320	-3.4072	0.06	1.5073	-3.6060
0.50	0.02	0.9218	-2.3338	0.04	0.9307	-2.5184	0.06	0.9386	-2.7098
0.75	0.02	0.4040	-1.5256	0.04	0.4347	-1.6897	0.06	0.4632	-1.8603
1.00	0.02	0.0071	-0.8161	0.04	0.0478	-0.9487	0.06	0.0864	-1.0876

Table 18. Interpretation of Nu and Sh with respect to H

η	H	Nu	Sh	H	Nu	Sh	H	Nu	Sh
0.00	2.0	2.1879	-4.4076	3.0	2.4463	-4.5965	4.0	2.7510	-4.8285
0.25	2.0	1.5195	-3.5057	3.0	1.6614	-3.5452	4.0	1.8263	-3.5978
0.50	2.0	0.9348	-2.6132	3.0	0.9288	-2.4627	4.0	0.9172	-2.2882
0.75	2.0	0.4492	-1.7742	3.0	0.3061	-1.4514	4.0	0.1380	-1.0798
1.00	2.0	0.0674	-1.7742	3.0	-0.1757	-0.5780	4.0	-0.4454	-0.0889

Table 19. Interpretation of Nu and Sh with respect to s

η	s	Nu	Sh	s	Nu	Sh	s	Nu	Sh
0.00	2.1	2.2425	-4.5466	2.2	2.2976	-4.6837	2.3	2.3533	-4.8227
0.25	2.1	1.5322	-3.5872	2.2	1.5445	-3.6655	2.3	1.5564	-3.7442
0.50	2.1	0.9253	-2.6549	2.2	0.9155	-2.6932	2.3	0.9055	-2.7318
0.75	2.1	0.4316	-1.7891	2.2	0.4143	-1.8010	2.3	0.3973	-1.8133
1.00	2.1	0.0510	-1.0144	2.2	0.0354	-1.0087	2.3	0.0204	-1.0033

Table 20. Interpretation of Nu and Sh with respect to Sr

η	Sr	Nu	Sh	Sr	Nu	Sh	Sr	Nu	Sh
0.00	0.5	2.1879	0.5288	1.0	2.1879	-0.0197	1.5	2.1879	-0.5682
0.25	0.5	1.5195	0.6057	1.0	1.5195	0.1489	1.5	1.5195	-0.3079
0.50	0.5	0.9348	0.6554	1.0	0.9348	0.2922	1.5	0.9348	-0.0710
0.75	0.5	0.4492	0.6746	1.0	0.4492	0.4025	1.5	0.4492	0.1304
1.00	0.5	0.0674	0.6622	1.0	0.0674	0.4755	1.5	0.0674	0.2889

5. CONCLUSIONS

The following lists the article's significant conclusions:

- The magnetic parameter, thermal Grashof number, and thermal diffusion parameter reduce the nanofluid primary and secondary velocity components.
- The solutal Grashof number, Darcy parameter, and Hall current parameter increase the nanofluid primary and secondary velocity components.

- The primary velocity declines and secondary velocity augments with an enhancement in the upper wall motion factor, rotation parameter, and heat generation parameters.
- The primary velocity maximizes, and the secondary velocity minimizes with an increase in the suction and volume fraction factors.
- The primary skin friction intensifies at the lower wall and declines at the upper wall by expanding the upper wall motion factor, rotation parameter, magnetic parameter, thermal Grashof number, and heat generation parameters.
- The primary skin friction declines at the lower wall and intensifies at the upper wall as the solutal Grashof number, Darcy parameter, Hall current parameter, thermal diffusion parameter, suction factor, and volume fraction factor are expanded.
- The secondary skin friction intensifies at the lower wall and declines at the upper wall by expanding the magnetic parameter, thermal Grashof number, suction factor, and volume fraction factor.
- The secondary skin friction declines at the lower wall and intensifies at the upper wall as the upper wall motion factor, rotation parameter, solutal Grashof number, Darcy parameter, Hall current parameter, thermal diffusion parameter, and heat generation parameter are expanded.

Nomenclature

u –	nanoliquid motion in x – direction	Sh –	mass transfer coefficient
v –	nanoliquid motion in y – direction	K^2 –	rotation parameter
w –	nanoliquid motion in z – direction	M –	magnetic parameter
a –	distance between two walls	s –	suction parameter
u_0 –	characteristic velocity	Gr –	thermal Grashof number
T –	nanoliquid temperature	Gm –	solutal Grashof number
T_0 –	cold wall temperature	Da –	Darcy parameter
t –	dimensional time	Pr–	Prandtl number
p –	nanoliquid pressure	Sr –	Soret number
V_0 –	suction velocity	H –	heat generation parameter
C –	nanoliquid species concentration	Sc –	Schmidt number
C_0 –	concentration at the cold wall	**Greek symbols**	
k_p –	permeability of the porous medium	Ω –	angular velocity
k_{nf} –	thermal conductivity of nanoliquid	ω –	non-dimensional frequency of oscillation
k_f –,	thermal conductivity of the base liquid	χ –	volume fraction of nanoliquid
k_s –	thermal conductivity of the solid	ρ_{nf} –	nanoliquid density
$(c_p)_{nf}$ –	specific heat of nanoliquid at stable pressure	μ_{nf} –	dynamic viscosity of nanoliquid
$(c_p)_f$ –	specific heat of the base liquid	μ_f –	dynamic viscosity of the base liquid
$(c_p)_s$ –	specific heat of the solid,	σ_{nf} –	electrical conductivity of nanoliquid
Q_0 –	dimensional heat generation parameter	σ_f –	electrical conductivity of the base fluid
D_m –	chemical molecular diffusivity	σ_s –	electrical conductivity of the solid
D_{nf} –	nanofluid mass diffusivity	β_{nf} –	thermal expansion coefficient of nanoliquid
T_m –	mean nanoliquid temperature	β_f –	thermal expansion coefficient of the base liquid
B_0 –	magnetic induction	β_s –	thermal expansion coefficient of the solid
m –	hall current factor	ρ_{nf} –	nanoliquid density
g –	acceleration due to gravity	ρ_f –	density of the base liquid
U –	nanofluid primary velocity	ρ_s –	density of the nanoparticle
W –	nanofluid secondary velocity	θ –	nanofluid temperature
n –	dimensional frequency of oscillation	ϕ –	species concentration
q_w –	heat flux	η –	A scaled coordinate
j_w –	mass flux	τ –	non-dimensional time
Cf –	skin friction coefficient	τ_e –	electron collision time
Pcf –	primary skin friction coefficient	τ_w –	shear stress
Scf –	secondary skin friction coefficient	ω_e –	cyclotron frequency
Nu –	heat transfer coefficient	λ –	upper wall motion parameter

Conflicts of interest
There is no conflict of interest disclosed by the writers.
Acknowledgements
It gives us great pleasure to convey our sincere gratitude to the reviewers for their insightful remarks and recommendations for improving this article.
Data availability
The text contains all the supporting information.
Funding
This manuscript was prepared without the assistance of any funding.

APPENDIX

$a_1 = \frac{1}{(1-\chi)^{2.5}}$, $a_2 = 1-\chi+\chi(\rho_s/\rho_f)$, $a_3 = 1+\left[3\chi(\sigma_s-\sigma_f)\right]\left[(\sigma_s+2\sigma_f)-\chi(\sigma_s-\sigma_f)\right]^{-1}$, $a_4 = 1-\chi+\chi\left[(\rho\beta)_s/(\rho\beta)_f\right]$

$a_5 = a_1a_2^{-1}$, $a_6 = a_3a_2^{-1}$, $a_7 = \left[(k_s+2k_f)-2\chi(k_f-k_s)\right]\left[(k_s+2k_f)+\chi(k_f-k_s)\right]^{-1}$, $a_8 = 1-\chi+\chi\left[(\rho c_p)_s/(\rho c_p)_f\right]$, $a_9 = a_7a_8^{-1}$,

$a_{10} = a_2\left[a_1\rho_f\right]^{-1}$, $a_{11} = S\Pr a_9^{-1}$, $a_{12} = H\Pr[a_8a_9]^{-1}$, $a_{13} = \Pr a_9^{-1}\left(Ha_8^{-1}-i\omega\right)$,

$a_{14} = a_7ScSr$, $a_{15} = \left[\exp(m_5)-\exp(-m_5)\right]^{-1}$, $a_{16} = \left[\exp(m_1)-\exp(m_2)\right]^{-1}$, $a_{17} = a_{14}a_{15}a_{16}$,

$a_{18} = m_1^2\left[\exp(m_1)-\exp(-m_5)\right]\left[m_1^2-m_5^2\right]^{-1}$, $a_{19} = m_2^2\left[\exp(m_2)-\exp(-m_5)\right]\left[m_2^2-m_5^2\right]^{-1}$, $a_{20} = a_{15}+a_{17}(a_{18}+a_{19})$,

$a_{21} = m_1^2\left[m_1^2-m_5^2\right]^{-1}$, $a_{22} = m_2^2\left[m_2^2-m_5^2\right]^{-1}$, $a_{23} = a_{14}a_{16}a_{21}$,

$a_{24} = a_{14}a_{16}a_{22}$, $a_{25} = a_{23}-a_{24}-a_{20}$, $a_{26} = \left[\exp(m_3)-\exp(m_4)\right]^{-1}$,

$a_{27} = m_3^2\left[m_3^2-Sc\,s\,m_3-Sc\,i\,\omega\right]^{-1}$, $a_{28} = m_4^2\left[m_4^2-Sc\,s\,m_4-Sc\,i\,\omega\right]^{-1}$, $a_{29} = a_{14}a_{26}a_{27}$,

$a_{30} = a_{14}a_{26}a_{28}$, $a_{31} = \left[\exp(m_7)-\exp(m_6)\right]^{-1}$, $a_{32} = a_{29}\left[\exp(m_3)-\exp(m_6)\right]$,

$a_{33} = a_{30}\left[\exp(m_4)-\exp(m_6)\right]$, $a_{34} = a_{31}(1+a_{32}-a_{33})$, $a_{35} = a_{29}-a_{30}-a_{34}$, $a_{36} = (a_6M)(1+im)^{-1}-2iK^2$, $a_{37} = a_{36}+(a_5/Da)$,

$a_{38} = sa_5^{-1}$, $a_{39} = a_{37}a_5^{-1}$, $a_{40} = \left[a_4(a_{16}Gr-a_{23}Gm)\right]\left[a_5(m_1^2-a_{38}m_1-a_{39})\right]^{-1}$, $a_{41} = \left[a_4(a_{17}Gr-a_{24}Gm)\right]\left[a_5(m_2^2-a_{38}m_2-a_{39})\right]^{-1}$,

$a_{42} = a_4a_{25}Gm\left[a_5(m_5^2+a_{38}m_5-a_{39})\right]^{-1}$, $a_{43} = a_4a_{20}Gm\left[a_5(m_5^2+a_{38}m_5-a_{39})\right]^{-1}$, $a_{44} = \lambda a_{36}a_5^{-1}a_{39}^{-1}$, $a_{45} = a_{40}-a_{41}+a_{42}+a_{43}-a_{44}$,

$a_{46} = a_{40}\exp(m_1)-a_{41}\exp(m_2)+a_{42}\exp(-m_5)+a_{43}\exp(m_5)-a_{44}+\lambda\cos(\omega\tau)$, $a_{47} = \left[\exp(m_8)-\exp(m_9)\right]^{-1}$,

$a_{48} = a_{47}\left[a_{46}-a_{45}\exp(m_9)\right]$, $a_{49} = a_{47}\left[a_{45}\exp(m_9)-a_{46}\right]$, $a_{50} = a_{37}+i\omega$, $a_{51} = a_{50}a_5^{-1}$,

$a_{52} = \left[a_4(a_{26}Gr-a_{29}Gm)\right]\left[a_5(m_3^2-a_{38}m_3-a_{51})\right]^{-1}$, $a_{53} = \left[a_4(a_{26}Gr-a_{30}Gm)\right]\left[a_5(m_4^2-a_{38}m_4-a_{51})\right]^{-1}$,

$a_{54} = a_4a_{35}Gm\left[a_5(m_6^2-a_{38}m_6-a_{51})\right]^{-1}$, $a_{55} = a_4a_{34}Gm\left[a_5(m_7^2-a_{38}m_7-a_{51})\right]^{-1}$, $a_{56} = a_{52}-a_{53}+a_{54}+a_{55}$,

$a_{57} = a_{52}\exp(m_3)-a_{53}\exp(m_4)+a_{54}\exp(m_6)+a_{55}\exp(m_7)$, $a_{58} = \left[\exp(m_{10})-\exp(m_{11})\right]^{-1}$, $a_{59} = a_{58}\left[a_{57}-a_{56}\exp(m_{11})\right]$,

$a_{60} = a_{58}\left[a_{56}\exp(m_{10})-a_{57}\right]$, $m_1 = 2^{-1}\left[a_{11}-\sqrt{a_{11}^2-4a_{12}}\right]$, $m_2 = 2^{-1}\left[a_{11}+\sqrt{a_{11}^2-4a_{12}}\right]$, $m_3 = 2^{-1}\left[a_{11}-\sqrt{a_{11}^2-4a_{13}}\right]$,

$m_4 = 2^{-1}\left[a_{11}+\sqrt{a_{11}^2-4a_{13}}\right]$, $m_5 = \sqrt{Scs}$, $m_6 = 2^{-1}\left[Sc\,s-\sqrt{(Sc\,s)^2+4Sc\,i\,\omega}\right]$, $m_7 = 2^{-1}\left[Sc\,s+\sqrt{(Sc\,s)^2+4Sc\,i\,\omega}\right]$,

$m_8 = 2^{-1}\left[a_{38}-\sqrt{a_{38}^2+4a_{39}}\right]$, $m_9 = 2^{-1}\left[a_{38}+\sqrt{a_{38}^2+4a_{39}}\right]$, $m_{10} = 2^{-1}\left[a_{38}-\sqrt{a_{38}^2+4a_{51}}\right]$, $m_{11} = 2^{-1}\left[a_{38}+\sqrt{a_{38}^2+4a_{51}}\right]$.

ORCID
Venkateswarlu Malapati, https://orcid.org/0000-0002-6320-0195; **Mohammed Almakki,** https://orcid.org/0000-0002-9348-4651; **V.B. Rajakumar Komaravolu,** https://orcid.org/0000-0002-2667-8042

REFERENCES

[1] D. O. Soumya, B. J. Gireesha, and P. Venkatesh, "Generalized Couette flow of nanoliquid among two concentric channels with particles injection," International Journal of Ambient Energy, **45**, Article 2353305 (2024). https://doi.org/10.1080/01430750.2024.2353305
[2] L. Swain, R. P. Sharma, and S. R. Mishra, "Diversified role of nanoparticle concentration and radiating heat on the natural convection Couette flow through a vertical channel," Colloid and Polymer Science, **302**, 1687-1700 (2024). http://dx.doi.org/10.1007/s00396-024-05294-3
[3] G. Ali, M. Ahmad, F. Ali, A. Khan, and I. Khan, "Couette flow of viscoelastic dusty fluid through a porous oscillating plate in a rotating frame along with heat transfer," Heat Transfer, **53**, 4588-4607 (2024). https://doi.org/10.1002/htj.23127
[4] M. Venkateswarlu, D.V. Lakshmi, O.D. Makinde, "Thermodynamics analysis of Hall current and Soret number on hydromagnetic Couette flow in a rotating system with a convective boundary condition, Heat Transfer Research," **51**, 83-101 (2020). https://doi.org/10.1615/HeatTransRes.2019027139

[5] S. L. Sun, D. Liu, C. Kang, H. B. Kim, Y. Z. Song, and P. G. Zhang, "Numerical simulation and machine learning study on heat transfer enhancement of nanofluids in Taylor–Couette flow with an elliptical slit surface," International Communications in Heat and Mass Transfer, **163**, Article 108788 (2025). https://doi.org/10.1016/j.icheatmasstransfer.2025.108788
[6] M. Venkateswarlu, P. Bhaskar, and O. D. Makinde, "Mathematical study of nonlinear mixed convection unsteady flow in a parallel plate inclined channel in the proximity of time periodic boundary conditions: flow reversal," Journal of Nanofluids, **10**, 598-607 (2021). https://doi.org/10.1166/jon.2021.1802
[7] R. Gupta, "Analyzing the impact of magnetic field, squeezing, and volume fraction on Magnetohydrodynamic nanofluid flow using a differential transform method," Journal of Nanofluids, **14**, 596-605 (2025). https://doi.org/10.1166/jon.2025.2261
[8] R. Arpitha, K. Ramesh, and D. Srikanth, "Temperature and mass dispersion of mixed convective MHD Casson nanofluid flow through porous medium," International Journal of Applied and Computational Mathematics, **11**, 1-25 (2025). https://doi.org/10.1007/s40819-025-01882-1
[9] F. S. Bayones, A. M. Abd-Alla, and E. N. Thabet, "Magnetized dissipative Soret effect on nonlinear radiative Maxwell nanofluid flow with porosity, chemical reaction and Joule heating," Waves in Random and Complex Media, **34**, 6270-6288 (2024). https://doi.org/10.1080/17455030.2021.2019352
[10] S. Mudoi, D. Sarma, and A. K. Sarma, "Newtonian fluid flow with heat and mass transfer across an inclined sheet and magnetic field with Soret effects," Journal of the Korean Physical Society, **86**, 280-291 (2025). https://doi.org/10.1007/s40042-024-01278-2
[11] H. Basha, N. B. Naduvinamani, and M, Shridhar, "Numerical analysis of velocity slip and magnetic Soret effect on dissipative Maxwell liquid motion about a stretching wall with heat source/sink," Numerical Heat Transfer, Part B: Fundamentals, **86**, 2721-2745 (2025). https://doi.org/10.1080/10407790.2024.2347613
[12] M. Venkateswarlu, P.R. Reddy, and K.J. Lakshmi, "Analytical study of Soret and Dufour effects on heat destructive Casson liquid movement past an infinite vertical plate," Journal of Naval Architecture and Marine Engineering, **21**, 27-40 (2024). https://doi.org/10.3329/jname.v21i1.69228
[13] P. Pandey, "Chemical reaction and heat source effects on oscillatory suction in MHD flow through permeable media with Soret effect," Aircraft Engineering and Aerospace Technology, **97**, 149-161 (2025). https://doi.org/10.1108/AEAT-01-2024-0023
[14] S. Jangid, and K. Kolla, "Magnetic field and Soret effect on mixed convection Williamson fluid model through a vertical channel using artificial neural network," International Journal of Numerical Methods for Heat & Fluid Flow, **35**, 4333-4365 (2025). https://doi.org/10.1108/HFF-10-2024-0781
[15] S. Ahamedsheriff, V. Rajaram, G. Mani, S. T. Thabet, and I. Kedim, "Impacts of soret and Dufour possessions on micropolar fluid past a stretching sheet in a porous medium," Scientific Reports, **15**, 33059 (2025). https://doi.org/10.1038/s41598-025-18302-5
[16] A. K. Sarma, D. Sarma, and S. Mudoi, "Magnetohydrodynamic flow and effects of Soret, Dufour and thermophoresis through a chemically reacting porous stretching plate," Sigma, **43**, 1533-1546 (2025). https://doi.org/10.14744/sigma.2025.00150
[17] M. Venkateswarlu, and D.V. Lakshmi, "Diffusion-thermo and heat source effects on the unsteady radiative MHD boundary layer slip flow past an infinite vertical porous plate," Journal of Naval Architecture and Marine Engineering, **18**, 55-72 (2021). https://doi.org/10.3329/jname.v18i1.33024
[18] M. Venkateswarlu, and D.V. Lakshmi, "Thermal diffusion, hall current and chemical reaction effects on unsteady MHD natural convective flow past a vertical plate," U. P. B. Sci. Bull., Series D: Mechanical Engineering, **79**, 91-106 (2017).
[19] O. D. Makinde, M. Venkateswarlu, and R. L. Monaledi, "Unsteady MHD flow of radiating and rotating fluid with Hall current and thermal diffusion past a moving plate in a porous medium," Defect and Diffusion Forum, **389**, 71-85 (2018). https://doi.org/10.4028/www.scientific.net/DDF.389.71
[20] S. Jayanthi, and H. Niranjan, "A vertical surface flow analysis of MHD nanofluids influenced by radiation, viscous dissipation, and joule heating with Soret and Dufour effects," Contemporary Mathematics, **5**, 2296-2314 (2024). https://doi.org/10.37256/cm.5220244318
[21] M. Venkateswarlu, and M. Phanikumar, "Soret and heat source effects on MHD flow of a viscous fluid in a parallel porous plate channel in presence of slip condition," U. P. B. Sci. Bull., Series D: Mechanical Engineering, **79**, 171-186 (2017).
[22] M. Venkateswarlu, and O. D. Makinde, Unsteady MHD slip flow with radiative heat and mass transfer over an inclined plate embedded in a porous medium, Defect and Diffusion Forum, **384**, 31-48 (2018). https://doi.org/10.4028/www.scientific.net/DDF.384.31
[23] Y. Ouyang, M.F.M. Basir, K. Naganthran, and I. Pop, "Exploring heat generation and magnetic effects on unsteady ternary nanofluid flow over a dynamic wedge in porous media," Chinese Journal of Physics, **93**, 531-548 (2025). https://doi.org/10.1016/j.cjph.2024.12.026
[24] S. Dey, S. Mukhopadhyay, and K. Vajravelu, "Thermo-solutal nonlinear convection in a nanofluid flow past a porous plate in the presence of heat generation/absorption," Heat Transfer, **54**, 1394-1419 (2025). https://doi.org/10.1002/htj.23221
[25] A. K. Hussein, S. E. Ahmed, M. A. Mansour, O. Younis, and L. Kolsi, "Effects of radiation and heat generation on MHD mixed convection in a double lid-driven inclined wavy porous cavity filled with non-Newtonian nanofluid and including a cross-shape heaters," Waves in Random and Complex Media, **35**, 5587-5614 (2025). https://doi.org/10.1080/17455030.2022.2071503
[26] M. Venkateswarlu, M. Phani Kumar, and O. D. Makinde, "Establishment of impulsive and accelerated motions of Casson fluid in an inclined plate in the proximity of MHD and heat generation," Periodica Polytechnica Mechanical Engineering, **66**, 219-230 (2022). https://doi.org/10.3311/PPme.19424
[27] Y. S. Daniel, Z. Ismail, P. Ayuba, S. Daniel, P. Anthony, P. N. Okolo, and A. S. Magaji, "Radiative heat transfer and Ohmic heating on unsteady EMHD mixed convective flow for dual stratified nanofluid," Modeling Earth Systems and Environment, **11**, 1-19 (2025). https://doi.org/10.1007/s40808-025-02387-y
[28] M. Z. Kefene, and E. H. Rikitu, "Magnetic and thermal radiation effects on hematocrit-dependent blood nanofluid flow in an inclined stenotic artery with heat generation," Brazilian Journal of Physics, **55**, 1-12 (2025). https://doi.org/10.1007/s13538-025-01770-5
[29] M. Venkateswarlu, P. Rami Reddy, and K. J. Lakshmi, "Nonlinear unsteady MHD flow in an inclined channel with suction and heat generation: time periodic boundary conditions," Journal of Naval Architecture and Marine Engineering, **22**, 199-216 (2025). https://doi.org/10.3329/jname.v22i2.75405

[30] M. S. Ram, M. D. Shamshuddin, C. Satyanarayana, and S. O. Salawu, "Stagnation point flow of magnetized convective nanofluid via porous stretchy surface subjected to ohmic heating and heat generation," International Journal of Modelling and Simulation, **45**, 1346-1360 (2025). https://doi.org/10.1080/02286203.2023.2281009
[31] M. Venkateswarlu, M. B. Chennaiah, and Md. Noor, "Significance of cross diffusion on the transient behavior of radiationg Casson fluid near a heated slanted plate," Bulletin of the Parana Mathematical Society, **43**, 1-19 (2025). https://doi.org/10.5269/bspm.78525
[32] Z. Abbas, S. Goher, and M. Y. Rafiq, "Interfacial flow and heat transfer analysis of kerosene–TiO_2 and water–Al_2O_3 nanofluids in shear-driven boundary layers," Journal of Engineering Research, (2025). https://doi.org/10.1016/j.jer.2025.12.001

ВПЛИВ СТРУМУ ХОЛЛА, ТЕПЛОВОГО РОЗСІЮВАННЯ ТА ТЕПЛОВИДІЛЕННЯ НА ПОТІК НАНОРІДИНИ TiO_2 НА ОСНОВІ ГАСУ ЧЕРЕЗ ОБЕРТОВИЙ ПОРИСТИЙ КАНАЛ

Венкатешварлу Малапаті[1], Мохаммед Алмаккі[2], В.Б. Раджакумар Комараволу[3]
[1]Кафедра математики, Академія вищої освіти Сіддхартхи, Віджаявада, Андхра-Прадеш, Індія - 520007
[2]Школа інженерії, архітектури та дизайну інтер'єрів, Університет Аміті, Міжнародне академічне місто Дубая, П.С. скринька 345019б Індія
[3]Кафедра математики, Технологічний інститут Каллама Харанадхаредді, Гунтур, Андхра-Прадеш, Індія - 522019

На відміну від тепловиділення та теплового розсіювання, досліджуються струм Холла та коефіцієнти обертання розряду нанорідини діоксиду титану на основі гасу через дві паралельні стінки, вбудовані в пористий канал. Розглядаються фактори всмоктування та гідромагнітні фактори. Використовуючи відповідні початкові та граничні умови, підхід збурень може дати точне аналітичне рішення для визначальних рівнянь для швидкості, температури та концентрації нанорідини. Можна отримати вирази для напруження зсуву, швидкості масопередачі та швидкості теплопередачі на пластинах. З одного боку, показано графічне представлення первинної та вторинної швидкостей, температури нанорідини та концентрації частинок. Однак, для різних значень відповідних коефіцієнтів течії, числові оцінки напруження зсуву, швидкості масопередачі та швидкості теплопередачі для стінок представлені у табличній формі. Через внесок сили плавучості розчиненої речовини, результуючі профілі первинної та вторинної швидкості постійно зростають до високого рівня. Концентрація збільшується разом зі збільшенням характеристик тепловиділення та теплодифузії по всій нанорідині. Коли сила теплової плавучості достатньо висока, профілі первинної та вторинної швидкості зменшуються. Струм Холла та параметр Дарсі підвищують коефіцієнти первинного та вторинного тертя поверхні на верхній стінці, одночасно зменшуючи їх на нижній. Однак на первинні та вторинні коефіцієнти тертя поверхні впливають протилежним чином сила теплової плавучості та магнітний параметр. Результати порівнюються з існуючою літературою.

Ключові слова: *нанорідина; потік Куетта; струм Холла; теплоутворення; відсмоктування*